A membrane-type acoustic metamaterial with adjustable acoustic properties

F. Langfeldt[a], J. Riecken[a], W. Gleine[a], O. von Estorff[b]

[a] *Department of Automotive and Aeronautical Engineering, Hamburg University of Applied Sciences, Berliner Tor 9, D–20099 Hamburg, Germany*
[b] *Institute of Modelling and Computation, Hamburg University of Technology, Denickestr. 17, D–21073 Hamburg, Germany*

Abstract

A new realization of a membrane-type acoustic metamaterial (MAM) with adjustable sound transmission properties is presented. The proposed design distinguishes itself from other realizations by a stacked arrangement of two MAMs which is inflated using pressurized air. The static pressurization leads to large non-linear deformations and, consequently, geometrical stiffening of the MAMs which is exploited to adjust the eigenmodes and sound transmission loss of the structure. A theoretical analysis of the proposed inflatable MAM design using numerical and analytical models is performed in order to identify two important mechanisms, namely the shifting of the eigenfrequencies and modal residuals due to the pressurization, responsible for the transmission loss adjustment. Analytical formulas are provided for predicting the eigenmode shifting and normal incidence sound transmission loss of inflated single and double MAMs using the concept of effective mass. The investigations are concluded with results from a test sample measurement inside an impedance tube, which confirm the theoretical predictions.

Keywords: metamaterial, membrane, transmission loss, non-linear, active

*Corresponding author
Email address: Felix.Langfeldt@haw-hamburg.de (F. Langfeldt)

Post-print submitted to Journal of Sound and Vibration *February 6, 2016*

Please cite as: Langfeldt, F., Riecken, J., Gleine, W. and O. von Estorff. A membrane-type acoustic metamaterial with adjustable acoustic properties. *Journal of Sound and Vibration* 373 (2016): 1–18. https://doi.org/10.1016/j.jsv.2016.03.025

1. Introduction

The so-called acoustic metamaterials have received much attention by researchers in physics and acoustical engineering during the last two decades. The term "metamaterial" has originally been coined in the late 1990s for composite materials specifically designed to yield physically unusual electromagnetic properties, such as negative permittivity and/or negative permeability [1]. Realizations of such extraordinary electromagnetic materials were proposed by Pendry et al. [2, 3] and first experimental evidence of metamaterials with negative permittivity and permeability was later provided by Smith et al. [4] and Shelby et al. [5], 30 years after Veselago [6] studied theoretically the physical consequences of such materials, such as negative refraction and a reversed Doppler effect. These findings initiated the emergence of a variety of electromagnetic metamaterials with powerful applications, e.g. a perfect lens overcoming the diffraction limit [7] or electromagnetic cloaks [8].

Light and sound waves are both governed by the wave equation. Therefore, most concepts of electromagnetic metamaterials can be transferred to acoustical problems. Consequently, Liu et al. [9] presented the first acoustic metamaterial with sub-wavelength-sized periodically arranged rigid spheres coated by an elastic material. This so-called locally resonant sonic material exhibited low-frequency bands with strongly reduced transmission of sound, caused by the effective density of the structure – i.e. the density "seen" by the acoustic wave passing through it – becoming negative in these band gaps [10]. Since then, many different types of acoustic metamaterials with negative density [11–16], negative bulk modulus [17–20], and double-negative properties [21–24] as well as various extraordinary applications of these metamaterials, like acoustic diodes [25], cloaks [26], near-unity absorbing surfaces [27], or acoustic superlenses [28], have been investigated.

From this wide range of different acoustic metamaterials developed by various research groups, the so-called membrane-type acoustic metamaterials (MAMs), originally proposed by Yang et al. [12], provide some features that are partic-

ularly useful in some engineering applications (e.g. aeronautical engineering), where lightweight structures and compact installation spaces are critical for the design of noise protection measures: MAMs are composed of thin pre-stressed membranes with one or more small rigid masses attached to the membrane material. These two-dimensional structures provide narrow frequency bands at low frequencies where the sound transmission through the MAM is reduced by several orders of magnitude below the corresponding mass-law [12, 29]. These frequency bands can be tuned during manufacturing of the MAM structures by choosing suitable values for the membrane pre-stress [30, 31], the magnitude of the added masses [12, 30, 31], the mass location [31–33], and the number of added masses [34, 35].

Once these parameters have been determined and the MAMs have been manufactured, however, it is not possible to re-tune the location of the high transmission loss frequency bands to account for shifting tonal components inside the spectrum of the noise source during operation (e.g. different rotational speeds of a propeller engine) or changes of the membrane pre-stress due to temperature changes or aging effects. There have been several efforts to increase the high transmission loss bandwidth using passive assemblies of MAMs: It is possible to stack multiple layers with differently tuned MAMs to achieve a broadband MAM panel with a high transmission loss over a wide frequency range that is more robust to changes in the operational conditions or material parameters [29, 36]. This, however, leads to a heavier structure requiring more installation space which might not be available in some applications. Alternatively, a single MAM layer with multiple MAM cells in a parallel arrangement and different added masses in each cell can be used to introduce multiple transmission loss peaks without increasing the size and weight of the MAM structure significantly [37, 38]. Nevertheless, this design also introduces additional resonances inside the frequency range of interest that may reduce the noise shielding capability of such a structure.

A substantially different approach to overcome the problematic narrow band characteristics of MAMs is to use active methods to adjust the MAM properties

during operation. Active acoustic metamaterials have first been investigated by Baz [39, 40] and Akl and Baz [41, 42], who used piezoelectric materials to tune the effective density and bulk modulus of acoustic metamaterials. On this basis, Popa et al. [43] developed a tunable active acoustic metamaterial with effective properties that can be adjusted over a wide range of values, which was later extended to realize an active acoustic diode [44]. Chen et al. [45] applied the principles of active acoustic metamaterials to MAMs by using a magnetorheological membrane material and an external gradient magnetic field to control the pre-stress inside the membrane material. This enables the shifting of the membrane eigenfrequencies during operation by selecting appropriate external magnetic field gradients. However, in the experiments by Chen et al. [45] a large permanent magnet was used to generate the required magnetic field, which greatly increases the overall mass and size of this active membrane-type metamaterial (AMAM). A different realization of an AMAM was recently proposed by Xiao et al. [46], who used a setup similar to that of a condenser microphone with an acoustically transparent fishnet electrode and the added mass on the MAM acting as the counter electrode. By applying an external DC voltage the eigenfrequency of the MAM could be decreased due to the additional attractive force between the electrodes. This new design requires the supply of a constant voltage in every unit cell of the AMAM. For possible fields of application, where a big surface needs to be covered with such AMAMs, large amounts of wiring are required for providing each unit cell with the suitable amount of voltage, thus increasing the mass and installation effort of the AMAM structures. Furthermore, in some cases it might be infeasible to use electrical wirings inside noise protection devices due to safety regulations.

To overcome the limitations of these designs, a new realization of an AMAM, that employs a centralized actuation principle for adjusting the dynamic MAM properties without requiring individual electrical circuits in each MAM unit cell, is presented in this contribution. The unit cell of the proposed AMAM is shown in Fig. 1. It consists of two vertically stacked MAMs that are mounted onto a frame. The MAMs investigated here have a square shape with one circular mass

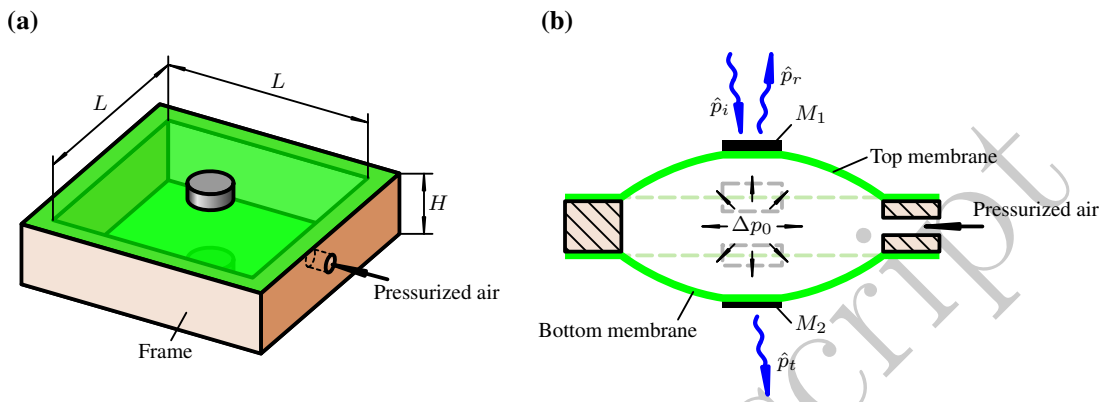

Figure 1: A unit cell of the proposed AMAM with an inflatable double MAM element. (a) Isometric view of the square AMAM unit cell; (b) Cross-sectional view through the AMAM unit cell.

attached in the center of each membrane layer. However, the basic principle of the proposed design can readily be applied to different MAM geometries (e.g. circular) and mass configurations (e.g. multiple masses per membrane layer). The materials of the membrane and the frame need to be airtight so that the air volume between the MAMs and the frame can be pressurized with a static differential pressure Δp_0 using an external source of pressurized air connected to the MAM by tubings or channels inside the frame. Pressurized air is usually readily available in passenger transport vehicles with air conditioning, such as trains or airplanes, which makes this concept particularly applicable to such fields of engineering. If Δp_0 is large enough, the deflection characteristic of the membranes due to the applied pressure difference becomes geometrically nonlinear and the stiffness of the membranes increases [47, 48]. This geometrical stiffening leads to an increase of the eigenfrequencies, which can be exploited to tune the acoustic properties of the double MAM element.

The present contribution is structured as follows: First, a theoretical analysis of the proposed AMAM based upon analytical and numerical models is presented to investigate the effect of the static inflation on the eigenfrequencies and, consequently, the normal incidence sound transmission loss (TL) of

the structure. Then, the results of an experimental investigation of the proposed AMAMs inside an impedance tube are presented in order to validate the theoretical predictions made in the first part of the paper.

2. Theoretical investigation

In this section a first theoretical investigation of the eigenfrequency shift and the adjustment of the normal incidence sound transmission loss by inflating the MAM is presented. In the first sub-section the shifting of the eigenfrequencies of a pre-pressurized MAM is examined using numerical simulations and an explicit equation for the eigenfrequency shifting is developed by performing a non-linear regression with the numerical results. The second sub-section deals with the effect of the pressurization on the eigenmode shapes of the MAM and the analytical calculation of the normal incidence sound transmission factor based upon the concept of effective surface mass density. In the final part of this section a theoretical model for the normal incidence sound transmission factor calculation of the inflatable double MAM element, as shown in Fig. 1, is presented and the results are compared to numerical simulation data.

2.1. Eigenfrequency shift of the inflated MAM

Previous investigations by other authors have shown that the large deflection of a membrane subjected to a uniform pressure difference Δp_0 leads to an overall increase of the in-plane stress resultant T inside the membrane [47, 48]. This phenomenon is known as geometrical stiffening and results in a shift of the eigenfrequencies f_i of the membrane to higher frequencies. A theoretical analysis by Plaut [47] has shown that the eigenfrequencies of a circular membrane are proportional to $\sqrt[3]{\Delta p_0}$ in the geometrically non-linear regime, where the static transversal deflection w_0 of the membrane is much larger than the membrane thickness t_m ($w_0 \gg t_m$). These findings for ordinary membranes motivate the assumption that the eigenfrequencies of a MAM undergoing large deflections due to a uniform static pressure difference Δp_0 are related to the eigenfrequencies of

the unpressurized MAM, denoted with $\bar{f}_i$, by an eigenfrequency shifting function ϕ_i:

$$f_i(\Delta p_0) \approx \phi_i(\Delta p_0)\bar{f}_i. \tag{1}$$

The eigenfrequency shifting function ϕ_i in Eq. (1) can be determined by performing a theoretical analysis of the non-linear static deflection of the pressurized MAM, taking into account the locally increased stiffness of the membrane in the area of the attached masses. Here, however, an empirical approach based upon numerically obtained results is adopted in order to obtain an explicit expression for ϕ_i to further investigate the effect of the eigenfrequency shifting on the transmission loss of the AMAM.

The non-linear deformation of a pressurized membrane leads to a somewhat complex non-linear stress state, where the in-plane stress resultant T is no longer homogenous across the membrane surface. In the case of rectangular membranes, which are considered in the present contribution, the in-plane stresses in the corners of the membrane can even be lower than before the pressurization [49]. This inhomogeneity of T inside a pressurized membrane affects each eigenmode of the membrane differently and therefore the frequency shifting function ϕ_i in Eq. (1) is expected to be different for every mode i in general.

From the theoretical model in Eriksson et al. [48] it can be deduced that the average in-plane stress resultant T_{av} inside a pressurized circular membrane is given by

$$T_{\mathrm{av}} = \bar{T}\left(1 + A\left(\frac{1}{\psi(\beta_0)} - \psi(\beta_0)\right)^2\right), \tag{2}$$

with the in-plane stress resultant of the unpressurized membrane $\bar{T}$, the non-dimensional static pressure load $\beta_0 = (\Delta p_0 L/\bar{T})\sqrt{E_m t_m(7-\nu_m)/(\bar{T}(1-\nu_m))}$, where L is a length scale of the membrane (i.e. the membrane radius, in case of a circular membrane), E_m and ν_m are the Young's modulus and Poisson ratio of the membrane material, respectively, and t_m is the membrane thickness. In this particular case the coefficient A equals to $A = (3-\nu_m)/(7-\nu_m)$ and the

function $\psi(\beta_0)$ is defined as

$$\psi(\beta_0) = \sqrt[3]{\sqrt{1 + B^2\beta_0^2} - B\beta_0}, \tag{3}$$

where B is another parameter that equals to $B = 0.1875$ for a circular membrane [48].

In order to obtain an explicit expression for the eigenfrequency shifting function ϕ_i, it is assumed that the squared eigenfrequencies of the pressurized MAM f_i^2 are following the same functional dependence on β_0 as the average in-plane stress resultant T_{av}, given by Eq. (2). The coefficients A and B given above, however, cannot be used for two reasons: First, the present contribution considers rectangular MAMs, i.e. rectangular membranes with attached small rigid masses, which are considerably different from the circular membranes investigated by Eriksson et al. [48]. Second, the non-homogenous part of the non-linear in-plane stress resultant T also affects the eigenfrequencies f_i for each eigenmode i differently. Hence, the coefficients A and B in Eqs. (2) and (3) are assumed to be dependent on both the membrane configuration and the mode index i, thus leading to the following form of the empirical frequency shifting function ϕ_i:

$$\phi_i(\beta_0) = \frac{f_i}{\bar{f}_i} = \sqrt{1 + A_i\left(\frac{1}{\psi_i(\beta_0)} - \psi_i(\beta_0)\right)^2}, \tag{4}$$

with

$$\psi_i(\beta_0) = \sqrt[3]{\sqrt{1 + B_i^2\beta_0^2} - B_i\beta_0} \tag{5}$$

and the coefficients A_i and B_i, which may be different for each MAM configuration and mode index i.

The unknown coefficients A_i and B_i in Eqs. (4) and (5) for the MAM configuration considered here are obtained from numerical simulations using the finite element method (FEM). The simulations have been performed to acquire the eigenfrequencies of the first two symmetric eigenmodes of the MAM, which have been shown to be most relevant for the low-frequency sound transmission through the MAM [50], at different pressure differences Δp_0. The basic setup of the numerical model is sketched in Fig. 2. The geometry and material of the

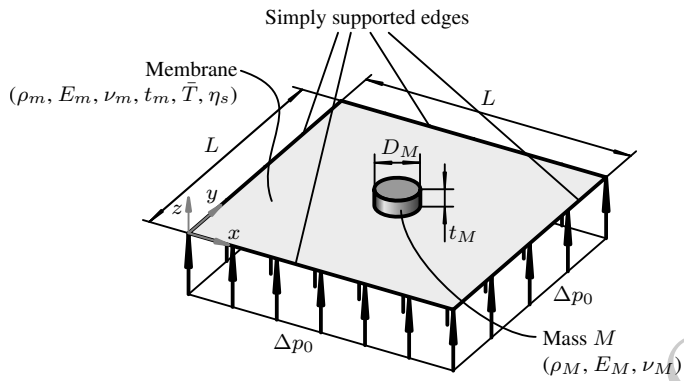

Figure 2: Setup of the finite element model for the determination of the eigenfrequencies of a MAM pressurized by a static differential pressure Δp_0.

square shaped membrane are chosen to be the same as the experimental test sample that was investigated in an impedance tube (see section 3). Hence, the MAM has an edge length of $L = 46$ mm and the edges of the membrane are assumed to be simply supported. The material that was used for the membrane is an iron-on film (Oracover), which is airtight and was pre-stressed by applying a temperature of 200 °C with a hot-air blower during manufacturing. A circular steel mass with a diameter of $D_M = 6$ mm and a thickness of $t_M = 2$ mm (resulting in a mass magnitude of $M = 0.45$ g) is attached to the membrane in the center of the MAM. Numerical values for the material properties of the membrane and mass, including the membrane pre-stress force resultant $\bar{T}$ and the structural loss factor η_s, used in all simulations for the present contribution are given in Table 1. The surface mass density of the membrane material is given by $m''_m = \rho_m t_m = 103\,\mathrm{g/m^2}$, which lies in the typical range of membrane materials used by other researchers in the context of MAMs, e.g. rubber ($m''_m = 274\,\mathrm{g/m^2}$, [12, 27]) or PEI ($m''_m = 91\,\mathrm{g/m^2}$, [30]). The total surface mass density of the MAM samples used in the present investigation is given by $m''_{\mathrm{tot}} = m''_m + M/L^2 = 316\,\mathrm{g/m^2}$. The resulting relationship between the static pressure differential Δp_0 acting on the MAM with the properties in Table 1 and the non-dimensional pressure difference β_0 is shown graphically in Fig. 3.

Table 1: Material properties of the MAM components that have been investigated in the numerical analysis.

Component	Material	ρ (kg/m^3)	E (GPa)	ν	t (mm)	$\bar{T}$ (N/m)	η_s
Membrane	Oracover	1450	2.5	0.4	0.071	235	0.02
Mass	Steel	7860	210	0.33	2	–	–

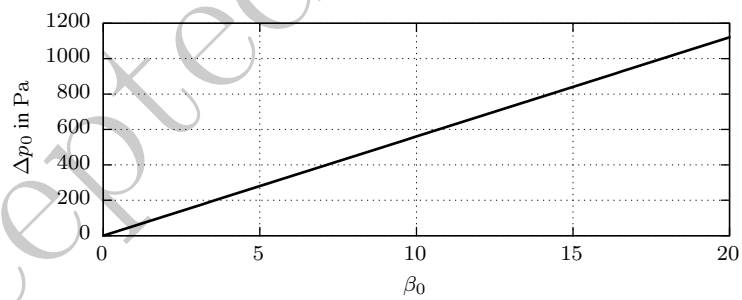

Figure 3: Numerical relation between the non-dimensional static pressure load β_0 and the actual value of the static differential pressure Δp_0 for the MAM sample configuration considered in the numerical simulations.

In order to investigate the influence of the mass diameter D_M on the frequency shifting, additional simulations with mass diameters of $D_M = 3$ mm and 12 mm have been performed. The density of the mass was adjusted to retain an added mass magnitude of $M = 0.45$ g. All other parameters were kept the same in these additional simulations.

The membrane was discretized using first-order triangular shell elements with an average edge length of $\Delta_m = 1$ mm, leading to nearly 5000 finite elements on the membrane. The added mass was discretized by first-order prismatic volume elements connected to the membrane via coincident nodes. A grid-sensitivity study showed that the selected element sizes delivered sufficiently accurate results.

The numerical procedure for obtaining the eigenfrequencies of the discretized MAM pressurized by a static pressure difference Δp_0 is as follows: First, the pre-stress inside the membrane material is applied by performing a linear static calculation of the membrane elements under a uniform temperature load of

$$\Delta\vartheta_m = -\frac{\bar{T}(1-\nu_m)}{E_m t_m \alpha_m}, \tag{6}$$

where the thermal expansion coefficient of the membrane material, without loss of generality, has been chosen as $\alpha_m = 1$ 1/K [51]. Then, the geometrically non-linear problem of the MAM loaded by a uniform static pressure difference Δp_0 is solved using an adaptive load stepping scheme with a full Newton-Raphson algorithm to iteratively determine the non-linear displacements of the MAM. In the final step, the differential stiffness matrix of the system, based upon the displacements due to the non-linear static preloading in the previous step, is calculated and used in a normal mode analysis to obtain the eigenmodes of the pressurized system.

The numerically obtained eigenfrequency shifts ϕ_i for the first two symmetric modes of the MAM with the three different mass diameters (given in non-dimensional form: $\delta_M = D_M/L = 0.065$, 0.13, and 0.261) are shown in Fig. 4. The non-dimensional pressure difference β_0 has been varied between 0 and 17.84, corresponding to a maximum Δp_0 of 1000 Pa (see Fig. 3). As

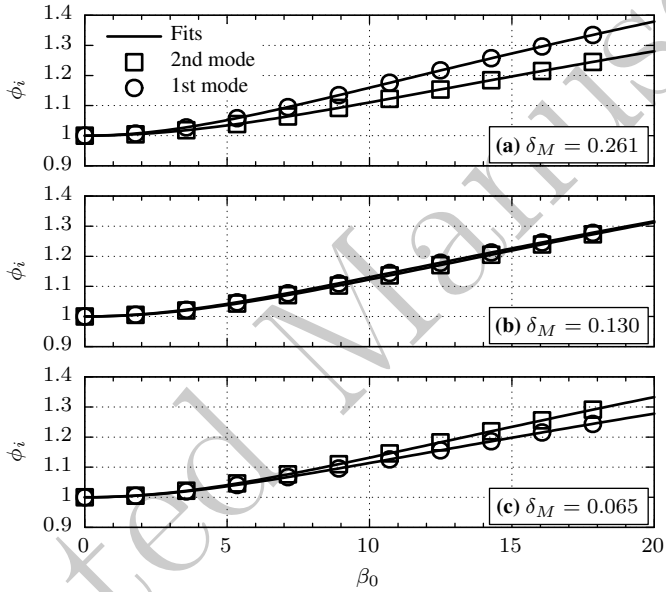

Figure 4: Eigenfrequency shift ϕ_i for the first two symmetric modes of the rectangular MAM shown in Fig. 2 with different non-dimensional mass diameters δ_M. The solid lines are the empirical frequency shifting functions $\phi_i(\beta_0)$ given in Eq. (4).

suggested by linear theory, the numerical results for all three mass diameters confirm that the frequency shifting is negligible at very low pressure differences β_0. For values of $\beta_0 > 2$, however, geometrical stiffening becomes dominant and the frequency shifting ϕ_i increases almost linearly with respect to β_0 within the investigated range of pressure differences, leading to frequency shifts of up to 35%. By comparing the results for the three different mass diameters in Fig. 4 it is evident that the sensitivity of the frequency shifting with respect to the pressure difference depends upon the mass diameter as well as the mode index i: For the largest mass diameter ($\delta_M = 0.261$), shown in Fig. 4a, the first eigenfrequency increases faster than the frequency of the second symmetric eigenmode of the MAM. In case of the smallest mass diameter ($\delta_M = 0.065$), as shown in Fig. 4c, however, this behavior is reversed with the second eigenfrequency rising faster than the first eigenfrequency. Assuming a continuous progression of the eigenfrequency shifting behavior between these two mass diameters it can be expected that there is a certain mass diameter, where the shifting behavior is the same for both eigenmodes. In fact, this is nearly the case for a non-dimensional mass diameter of $\delta_M = 0.13$, shown in Fig. 4b, where the eigenfrequencies of both modes are shifted equally. Hence, in this particular case the frequency shifting function ϕ_i is, at least for the first two symmetric eigenmodes, which are most relevant for the low-frequency transmission loss of MAMs, independent of the mode index i.

Based upon the numerical results shown in Fig. 4, non-linear regression analyses have been performed for each non-dimensional mass diameter δ_M and mode index i to determine the coefficients A_i and B_i in the empirical frequency shifting function Eq. (4). The resulting functions are shown as solid curves in Fig. 4 and the corresponding numerical values of the coefficients are given in Table 2. The summed squares of residuals were less than 10^{-6} for all curve fits, which indicates that the empirically chosen frequency shifting function in Eq. (4) yields very good agreement with the numerical simulations inside the investigated range of pressure differences as observed in Fig. 4.

When comparing the numerical values for the coefficients A_i and B_i, given in

Table 2: Numerical values for the coefficients A_i, B_i, and C_i in Eqs. (4) and (18) for different non-dimensional mass diameters δ_M.

First mode			
δ_M	0.065	0.13	0.261
A_1	0.4787	0.5571	0.6788
B_1	0.1242	0.1237	0.1248
C_1	1.354	1.0069	0.6036
Second mode			
δ_M	0.065	0.13	0.261
A_2	0.7262	0.6727	0.5755
B_2	0.1052	0.1055	0.1084
C_2	0	0	0

Table 2, it can be seen that both coefficients are affected differently by the mass diameter δ_M and the mode index i: A_1 and A_2 are depending on the dimensionless mass diameter δ_M in different directions. In case of the first mode, A_1 is increasing with increasing mass diameter, which indicates that the frequency shifting of the first eigenfrequency becomes less pronounced for smaller masses (as observed in Fig. 4). For the coefficient A_2 of the second mode's eigenfrequency shifting function this behavior is inverted. The coefficients B_1 and B_2, on the other hand, are nearly independent of the mass diameter with a relative standard deviation of less than 2%. Hence, the mean values $\bar{B}_1 = 0.1242$ and $\bar{B}_2 = 0.1064$ can be used for all δ_M inside the investigated range of mass diameters to yield a sufficiently accurate representation of the frequency shifting function ϕ_i.

The different behavior of the coefficients A_i and B_i with respect to the mass diameter, as given in Table 2, can be interpreted physically as follows: The coefficient B_i in Eq. (5) serves as a scaling factor for the non-dimensional pressure

difference β_0. Hence, for a given value of β_0, the value of the bracketed term in Eq. (4) increases as the value of B_i increases. Since B_i is nearly independent of the mass diameter within the investigated range of diameters, it can be understood as a mode-dependent non-linearity parameter. In case of the non-linear loading of an annular membrane, the highest stresses are found at the inner radius [52]. Hence, for the rectangular MAM with circular added mass it can be expected that the highest stresses are found at the circumference of the mass. In the first symmetric eigenmode of the MAM the vibration of the added mass dominates the mode shape, while in the second symmetric MAM eigenmode the added mass is nearly at rest (see Fig. 6). Thus, the increased stress at the mass circumference caused by the pressurization of the MAM leads to an increase of the effective stiffness for the mass-dominated first eigenmode, while the effect on the second eigenmode is smaller. This is reflected by the coefficients B_1 and B_2, with $B_1 > B_2$ indicating that the effect of the pressurization on the first eigenfrequency is larger than on the second eigenfrequency.

Since the coefficient B_i does not change with the mass diameter, the influence of δ_M is reflected in the variation of the parameter A_i in Table 2. For the first eigenmode, the numerical values of A_1 increase as the mass diameter gets larger. From Eq. (4) it can be deduced that this leads to a stronger eigenfrequency shifting as observed in Fig. 4. This can again be explained by considering the pressurized MAM approximately as a non-linearly deformed annular membrane. Plaut [52] has shown that in this case the stress at the inner radius increases as the inner radius increases. From this it can be deduced that a large mass radius leads to larger stresses at the mass circumference which in turn results in a larger shifting of the first eigenfrequency as indicated by the variation of A_1 in Table 2. In case of the second mode, on the other hand, a reduction of the eigenfrequency shifting is observed in Fig. 4 as the mass diameter increases. The coefficient A_2 in Table 2 reflects this behavior with decreasing values for increasing mass diameters. It is possible that this is a consequence of the rectangular shape of the MAM: As mentioned above, pressurized rectangular membranes exhibit reduced in-plane stresses at the corners [49]. Thus, the membrane stiffness is reduced

in these particular regions. Since the second MAM mode is characterized by strong vibrations of the membrane material with the added mass being mostly at rest, this stiffness reduction diminishes the eigenfrequency shifting of the second mode. For larger masses the corner regions with reduced stiffness become more significant for the remaining unloaded membrane surface. Therefore, the frequency shifting of the second mode and, consequently, the values for the coefficient A_2 are reduced as the mass diameter increases.

2.2. Transmission factor of the inflated MAM

In order to investigate the effect of the shifted eigenfrequencies on the sound transmission properties of the inflated MAM, the normal incidence sound transmission factor t of the structure is calculated using the effective surface mass density $\widetilde{m}''$, which is defined as [12, 33]:

$$\widetilde{m}'' = \frac{\langle \Delta \hat{P} \rangle}{\langle \hat{a}_z \rangle} = \frac{\langle \Delta \hat{P} \rangle}{-\omega^2 \langle \hat{w}_z \rangle}, \tag{7}$$

where $\Delta \hat{P}$ is the amplitude of the harmonic sound pressure difference along the membrane surface, $\hat{a}_z = -\omega^2 \hat{w}_z$ is the vibrational acceleration amplitude in normal direction of the membrane surface, $\hat{w}_z$ is the vibrational displacement amplitude, and

$$\langle v \rangle = \frac{1}{S} \int_S v \, \mathrm{d}S \tag{8}$$

denotes the surface average of a quantity v performed over the membrane surface S. The normal incidence sound transmission factor t, defined as the pressure amplitude ratio of the transmitted and incident sound wave, is obtained from the effective surface mass density of the MAM $\widetilde{m}''$ by applying the well-known mass law relationship:

$$t = \frac{1}{1 + \frac{\mathrm{i}\omega \widetilde{m}''}{2\rho_0 c_0}}, \tag{9}$$

where ρ_0 and c_0 are the density and speed of sound of the surrounding medium, respectively. The normal incidence sound transmission loss is then given by

$$\mathrm{TL} = -20 \log |t| = 20 \log \left| 1 + \frac{\mathrm{i}\omega \widetilde{m}''}{2\rho_0 c_0} \right|. \tag{10}$$

For the theoretical investigations in the present contribution, Eq. (7) is transformed into the non-dimensional form

$$\frac{\widetilde{m}''}{m''_m} = -\frac{\beta}{\nu^2}\frac{1}{\langle u \rangle}, \tag{11}$$

where $\beta = \Delta\hat{P}L/\bar{T}$ is the non-dimensional acoustic pressure difference along the membrane surface, which is constant, because only normally incident sound waves are considered here, $\nu^2 = (m''_m/\bar{T})\omega^2 L^2$ is the squared non-dimensional frequency, and $u = \hat{w}_z/L$ is the non-dimensional membrane displacement amplitude. The non-dimensional components of the membrane coordinate system (see Fig. 2) are given by $\xi = x/L$, $\eta = y/L$, and $\zeta = z/L$, so that the non-dimensional surface averaged membrane displacement amplitude in Eq. (11) becomes

$$\langle u \rangle = \int_0^1 \int_0^1 u(\xi, \eta)\, \mathrm{d}\xi\, \mathrm{d}\eta. \tag{12}$$

According to Yang et al. [50], the effective surface mass density in Eq. (7) can be rewritten in terms of the eigenfunctions $\Phi_i(\xi, \eta)$ of the MAM as

$$\frac{\widetilde{m}''}{m''_m} = -\frac{1}{\nu^2 \sum\limits_{i=1}^{\infty} \frac{R_i}{\nu_i^2 - \nu^2}}, \tag{13}$$

where structural damping of the membrane material has been neglected, ν_i are the non-dimensional eigenfrequencies f_i, and the residuals R_i are related to the MAM eigenfunctions Φ_i in the following way:

$$R_i = \frac{\langle \Phi_i \rangle \langle \Phi_i^* \rangle}{\langle \Phi_i \mu'' \Phi_i^* \rangle}, \tag{14}$$

where Φ_i^* denotes the complex conjugate of the eigenfunction Φ_i, μ'' is the dimensionless surface mass density distribution along the membrane surface, defined as

$$\mu'' = \begin{cases} 1 & \text{on the membrane surface} \\ 1 + \mu''_M & \text{on the mass surface,} \end{cases} \tag{15}$$

and $\mu''_M = M/(0.25\pi D_M^2 m''_m)$. The infinite series in the denominator of Eq. (13) is truncated after a sufficient number of eigenmodes K. Thus, Eq. (13) can be

written in matrix form as

$$\frac{\widetilde{m}''}{m''_m} = -\frac{1}{\nu^2\ \mathbf{r}^T(\mathbf{\Lambda} - \nu^2\mathbf{I})^{-1}\mathbf{r}}, \tag{16}$$

where $\mathbf{r}^T = \left(\sqrt{R_1}, \ldots, \sqrt{R_K}\right) \in \mathbb{R}^K$, $\mathbf{\Lambda} \in \mathbb{R}^{K\times K}$ is a diagonal matrix with the squared non-dimensional eigenfrequencies ν_i^2, and $\mathbf{I}$ is the K by K identity matrix.

It can be expected that, due to the inhomogenous stress distribution inside the non-linearly deformed MAM, the eigenfunctions Φ_i, just like the eigenfrequencies f_i, are depending on the static pressure difference load Δp_0. Consequently, the residuals R_i in Eq. (13) are a function of β_0 and can be expressed in terms of the residuals of the unpressurized MAM, $\bar{R}_i$, via a residual shifting function $\chi_i(\beta_0)$ as

$$R_i(\beta_0) = \chi_i(\beta_0)\bar{R}_i. \tag{17}$$

To analyze the influence of the static pressurization on the modal residuals R_i of the MAM, the residual shifts χ_i are calculated from the eigenfunctions Φ_1 and Φ_2 that have been obtained from the numerical modal analysis described in the preceding section. The results are provided in Fig. 5 for the same three mass diameters that were investigated in Fig. 4. It can be seen that in all three cases the modal residual of the first eigenmode of the MAM is reduced with increasing pressure difference β_0. Furthermore, the numerical simulations indicate that this effect becomes more pronounced as the mass diameter decreases, with the residuals being reduced to almost 60 % at $\beta_0 = 17.84$ in case of the smallest investigated mass diameter $\delta_M = 0.065$. The residuals of the second mode, on the other hand, are nearly unaffected by the pressurization – the residual shift χ_2 is near unity in all three mass diameter cases. This indicates that the eigenfunction of the first mode Φ_1 is significantly altered as a result of the inflation, while the second mode eigenfunction Φ_2 is the same, regardless of the applied external pressure (at least within the investigated pressurization range). These findings are confirmed in Fig. 6, where, for the medium-sized mass with $\delta_M = 0.13$, the first two mode shape functions Φ_1 and Φ_2 at $\eta = 0.5$

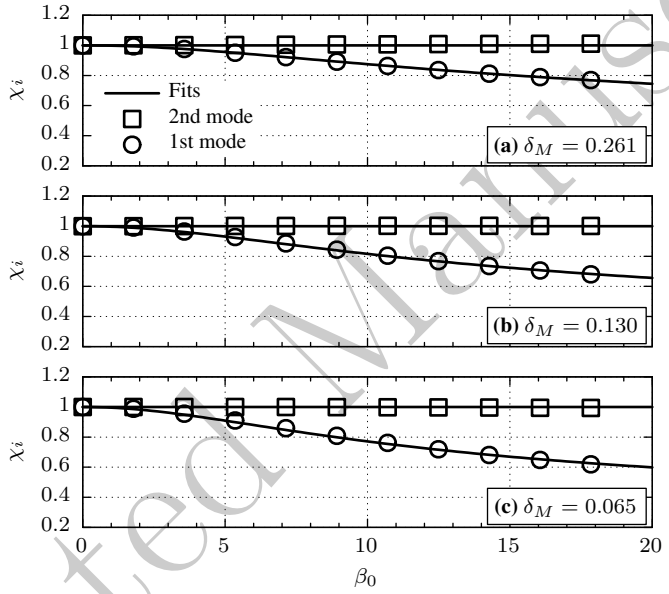

Figure 5: Residual shift χ_i for the first two symmetric modes of the rectangular MAM shown in Fig. 2 with different non-dimensional mass diameters δ_M. The solid lines are the empirical frequency shifting functions $\chi_i(\beta_0)$ given in Eq. (18).

are shown for the unpressurized case ($\beta_0 = 0$) and the largest investigated static pressure difference ($\beta_0 = 17.84$). In case of the first mode shape function Φ_1, the pressurization leads to an elongated shape with the membrane displacement dropping off much steeper between the mass (where the displacement is the largest for this mode) and the membrane edges. The second mode shape function Φ_2, however, does not change much as a result of the inflation. Consequently, the residual shift for the second mode is $\chi_2 \approx 1$, as has been observed in Fig. 5.

A more detailed analysis of the first mode residual shifts in Fig. 5 reveals that the reciprocal value of χ_1 follows the same qualitative dependence on β_0 as the corresponding frequency shift ϕ_1. Therefore, a reasonable ansatz for a residual shifting function $\chi_i(\beta_0)$ takes the following form:

$$\chi_i(\beta_0) = \frac{R_i}{\bar{R}_i} = \frac{1}{\sqrt{1 + C_i \left(\frac{1}{\psi_i(\beta_0)} - \psi_i(\beta_0) \right)^2}}, \tag{18}$$

where C_i is a coefficient, depending on the mode index i and mass diameter δ_M, and $\psi_i(\beta_0)$ is given by Eq. (5).

The coefficient C_1 in Eq. (18) for the first mode is determined by performing a non-linear regression analysis with the numerical data shown in Fig. 5. Since the second mode residuals are nearly unaffected by the pressurization of the MAM, C_2 is set to zero, so that $\chi_2(\beta_0) = 1$. The resulting numerical values for C_1 and C_2 are given in Table 2 and the corresponding curves are shown as solid lines in Fig. 5 for comparison with the simulation results. Eq. (18) provides a reasonably good agreement with the FEM results for the first mode, where a strong dependence of the residuals on β_0 has been observed, as well as the second mode, where $\chi_2(\beta_0) \approx 1$.

The effective mass density $\widetilde{m}''$ of the inflated MAM, given by Eq. (16), can now be formulated in terms of the unpressurized MAM eigenfrequencies $\bar{\mathbf{\Lambda}}$ and residuals $\bar{\mathbf{r}}$:

$$\frac{\widetilde{m}''}{m''_m} = -\frac{1}{\nu^2\, \bar{\mathbf{r}}^T \mathbf{X} \left(\mathbf{\Phi}^2 \bar{\mathbf{\Lambda}} - \nu^2 \mathbf{I} \right)^{-1} \mathbf{X} \bar{\mathbf{r}}}, \tag{19}$$

where $\mathbf{X} = \mathrm{diag}(\sqrt{\chi_1}, \ldots, \sqrt{\chi_K})$ and $\mathbf{\Phi} = \mathrm{diag}(\phi_1, \ldots, \phi_K)$. The expression in Eq. (19) shows that two different mechanisms are responsible for manipulating

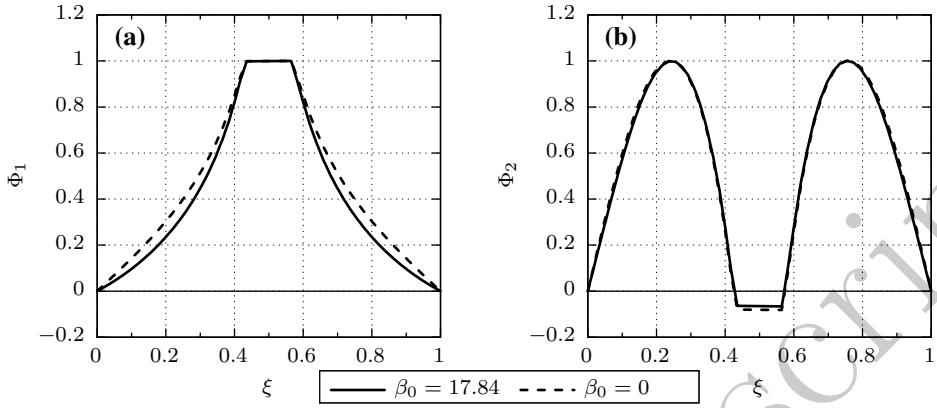

Figure 6: Simulated mode shapes of the first two symmetric MAM eigenmodes with $\delta_M = 0.13$ at $\eta = 0.5$ for the non-dimensional pressure differences $\beta_0 = 17.84$ (1000 Pa pressurization, solid lines) and $\beta_0 = 0$ (no pressurization, dashed lines). The mode shape functions are scaled with the corresponding maximum value. (a) Mode 1; (b) Mode 2.

the effective surface mass density and, via the relationships in Eqs. (9) and (10), the sound transmission properties of the inflatable MAM: The eigenfrequency shifting $\mathbf{\Phi}$, as discussed in the previous sub-section, directly affects the zeros of the effective surface mass density in Eq. (19), i.e. the eigenfrequencies of the inflated MAM where the transmission loss goes to zero. The peak frequencies ν_P, i.e. the frequencies where $\widetilde{m}''$ and the transmission loss TL go to infinity, on the other hand, are influenced by both the eigenfrequency shifting and the residual shifting, denoted by the diagonal matrix $\mathbf{X}$. In general, the peak frequencies can be obtained from solving the equation

$$\bar{\mathbf{r}}^T \mathbf{X} \left(\mathbf{\Phi}^2 \bar{\mathbf{\Lambda}} - \nu_P^2 \mathbf{I} \right)^{-1} \mathbf{X} \bar{\mathbf{r}} = \sum_{i=1}^{K} \chi_i \frac{\bar{R}_i}{\phi_i^2 \bar{\nu}_i^2 - \nu_P^2} \stackrel{!}{=} 0, \tag{20}$$

which shows that there is a somewhat complex relationship between the peak frequencies ν_P and the modal eigenfrequency and residual shifts ϕ_i and χ_i.

To analyze the shifting of the first peak frequency ν_{P1}, finite element simulations of the normal incidence sound transmission through the pressurized MAM have been performed. A general overview of the model setup is given in Fig. 7. The finite element model consists of the same MAM model that was used for the

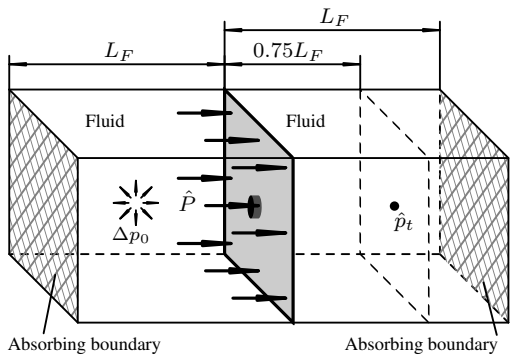

Figure 7: Setup of the finite element model for the calculation of the normal incidence sound transmission factor t of a MAM pressurized by a static differential pressure Δp_0.

normal modes analysis in the previous section (see Fig. 2) with a mass diameter of $D_M = 6$ mm. A fluid cavity with a length of $L_F = L = 46$ mm is attached to each side of the MAM and terminated by absorbing elements. The cavity side walls are assumed to be sound hard in order to provide the same conditions as inside an impedance tube. The fluid volume is discretized using tetraeder elements with an average element edge length of $\Delta_f = 5$ mm. Full vibro-acoustic coupling between the membrane and the fluid elements is ensured by using coincident grid points at the fluid-structure interfaces. The density and speed of sound of the fluid are $\rho_0 = 1.225$ kg/m^3 and $c_0 = 340$ m/s, respectively, corresponding to standard values of air at sea level. The first two steps of the analysis procedure (temperature load for pre-stressing and non-linear static pressure load with Δp_0) are the same as in the normal modes analysis described in the previous sub-section. In the final step, however, a direct frequency response of the MAM under a harmonic uniform pressure load with amplitude $\hat{P}$ is calculated for frequencies ranging from $f = 100$ to 1000 Hz. This approach yields normally incident plane acoustic waves inside the fluid cavities and therefore the amplitude of the transmitted wave $\hat{p}_t$ is extracted from a field point at a distance of $0.75L_F$ away from the membrane surface. Thus, the normal incidence sound

transmission factor is given by

$$t = \frac{\hat{p}_t}{0.5\hat{P}} e^{\mathrm{i}k_0 0.75 L_F}, \tag{21}$$

where $k_0 = \omega/c_0$ is the acoustic wave number. It has to be noted that the investigated range of static pressurizations ($\Delta p_0 = 0 \ldots 1$ kPa) is two orders of magnitudes lower than the static pressure of the ambient air ($p_0 = 101.15$ kPa) and the pressurization process is assumed to be isothermal. Hence, the speed of sound c_0 is constant in the pressurized air volume and the density ρ_0 increases by only up to 1 %. Therefore, the characteristic impedance of the fluid $Z_0 = \rho_0 c_0$ is assumed to be equal on both sides of the MAM, even when the pressurization is applied.

Additionally to the numerical simulations the normal incidence sound transmission factor has been calculated analytically by using Eq. (19) and the empirical eigenfrequency and residual shifting functions in Eqs. (4) and (18) with the corresponding numerical values for the coefficients given in Table 2 to obtain the effective surface mass density $\widetilde{m}''$ of the MAM. The unshifted non-dimensional eigenfrequencies $\bar{\nu}_i$ and residuals $\bar{R}_i$ of the first $K = 2$ symmetric eigenmodes of the MAM are calculated using an analytical model for MAMs, which employs a point-matching approach to couple the membrane vibration with the mass vibration and expands the membrane displacement in the eigenfunctions of the membrane without added masses [33]. To account for the bending stiffness of the membrane material, the analytical model has been extended to include this effect into the assembly of the stiffness matrix for the calculation of the MAM eigenmodes.

The transmission loss results for the investigated inflatable MAM configuration are shown in Fig. 8a at three different pressure difference levels $\beta_0 = 0$ (unpressurized), $\beta_0 = 8.92$ ($\Delta p_0 = 500$ Pa), and $\beta_0 = 17.84$ ($\Delta p_0 = 1000$ Pa). Additionally, the phase of the calculated complex sound transmission factors is given in Fig. 8b. The lines correspond to the analytically obtained results using Eq. (19) and the symbols are the results from the numerical simulation. Both analytical and numerical results for the transmission loss as well as the trans-

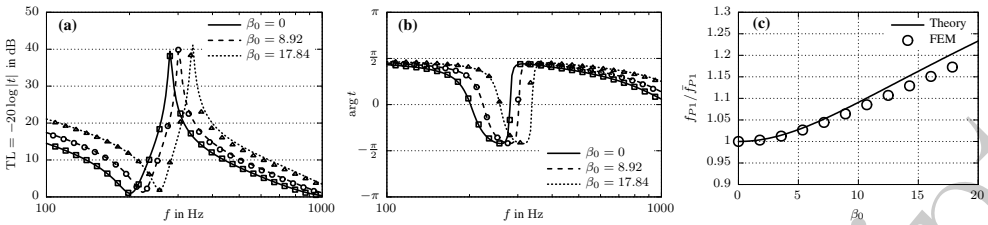

Figure 8: Analytical results (lines) and numerical results (symbols) for the single MAM at different inflation pressure differences β_0. (a) Normal incidence sound transmission loss; (b) Phase of the sound transmission factor t; (c) Shifting of the first transmission loss peak frequency f_{P1}.

mission factor phase show very good agreement with each other. Especially in the unpressurized case both methods yield identical results, which shows that the first two symmetric modes are sufficient for the analytical transmission loss calculation. For $\beta_0 > 0$ small deviations between both methods become visible, most notably around the transmission loss peaks, where the shifting of the peaks is slightly overestimated by the analytical calculations. This can be explained by the fact that the eigenfrequency and residual shifting functions in Eqs. (4) and (18), respectively, have been obtained by a non-linear regression method, which, especially in the case of the residual shifting function shown in Fig. 5, introduces some error into the analytical predictions. This error, however, is acceptable, because the deviations of the analytical and numerical results are within acceptable bounds. When comparing the transmission loss results in Fig. 8a for the three different pressure differences, it becomes apparent that the pressurization of the MAM leads to a nearly uniform shifting of the whole transmission loss spectrum to higher frequencies. This shifting is not perfectly uniform, because the relative shifting of the transmission loss peak is not as large as compared to the shifting of the two eigenfrequencies. The same shifting effect can be observed for the phase of the sound transmission factor t, as shown in Fig. 8b.

Fig. 8c shows the shifting of the first peak frequency f_{P1} in dependence of the non-dimensional pressure difference β_0. When comparing this plot with the

eigenfrequency shifts shown in Fig. 4b, it can be seen that at e.g. $\beta_0 = 17.84$ the eigenfrequencies are shifted by 28 %, while the first peak frequency is increased by only 17 % (or 20 %, in case of the analytical results). The reason for this different behavior is found in the residual shifting χ_i, which does not affect the eigenfrequencies of the MAM, but tends to retard the shifting of the transmission loss peak.

In summary, the results presented in this sub-section show that the pressurization of a MAM is a suitable method for adjusting the transmission loss peak of the MAM during operation. The shifting is nearly linear above a certain value of the non-dimensional pressure difference β_0 and can be estimated fairly accurately with the effective surface mass density in Eq. (19) and suitable eigenfrequency and residual shifting functions (Eqs. (4) and (18)).

2.3. Transmission factor of the inflated double MAM

In most potential application fields for inflatable MAMs it is not feasible to pressurize a large air volume on one side of the MAM in order to create the static pressure difference Δp_0. Therefore, a double AMAM structure, as shown in Fig. 1, is proposed, where two MAMs are separated vertically by a frame of height H and the enclosed air volume is pressurized to inflate both MAMs simultaneously. In addition, further benefits of this configuration are the increased reduction of sound transmission due to the stacking of two MAMs [36] and that both MAM layers can be tuned differently (i.e. by choosing different added masses M_1 and M_2) to create two different transmission loss peaks, which can be adjusted during operation by the inflation mechanism.

As shown in Appendix A, the normal incidence sound transmission factor of the double MAM arrangement at low frequencies can be obtained by treating the system as a double wall with the two non-dimensional wall impedances

$$X_1 = \frac{\mathrm{i}\omega \widetilde{m}_1''}{2\rho_0 c_0} \quad \text{and} \quad X_2 = \frac{\mathrm{i}\omega \widetilde{m}_2''}{2\rho_0 c_0}, \tag{22}$$

where $\widetilde{m}_1''$ and $\widetilde{m}_2''$ are the effective surface mass density (see Eq. (19)) of the top and bottom MAM layer, respectively. Taking into account the impedance of the

fluid cavity between the two MAMs, the normal incidence sound transmission factor is given by [53]

$$t = \frac{1}{1 + X_1 + X_2 + X_1 X_2 \left(1 - e^{-2\mathrm{i}k_0 H}\right)}. \tag{23}$$

At low frequencies the MAM spacing H typically is much smaller than the acoustic wavelength ($k_0 H \ll 1$), so that Eq. (23) can be simplified into the following low-frequency approximation form:

$$t = \frac{1}{1 + X_1 + X_2 + 2\mathrm{i}k_0 H X_1 X_2}. \tag{24}$$

Finite element simulations of the normal incidence sound transmission factor through an inflatable double MAM element are used to evaluate the results from the analytical model given by Eq. (24). It is possible to calculate the sound transmission properties of the given coupled double MAM structure with the method developed by Yang et al. [50] using only the first few eigenmodes of a double MAM element. In order to verify the analytical double MAM model, however, the numerical setup is chosen to be mostly identical to the setup for the single MAM model (see Fig. 7). In this case, two MAMs with identical properties according to Table 1 separated by an air gap of height $H = 15$ mm are analyzed inside the rectangular acoustic waveguide. This way, a direct frequency response algorithm can be employed in the simulations and possible errors due to the modal truncation in the analytical model can be evaluated by comparing both analytical and numerical results.

The calculated results are shown in Fig. 9 for the same three non-dimensional pressure differences β_0 as already shown in Fig. 8 for the single MAM. The lines represent the analytical data and the symbols correspond to the simulation results. In the unpressurized case ($\beta_0 = 0$, solid line/square symbols) the transmission loss is greatly increased by the stacked MAM arrangement with peak values greater than 60 dB, which confirms the results of previous investigations on stacked MAMs [36]. Apart from the two resonance frequencies corresponding to the single MAM resonances visible as minima of the transmission loss at 200 Hz and 1100 Hz (outside the range of Fig. 8a), an additional resonance

appears at a frequency slightly below the peak frequency. This resonance can be attributed to the monopole resonance of the coupled double MAM system, as discussed in [54], while the other two resonances are the dipole resonances of the system. The analytical and numerical results for the transmission loss TL (Fig. 9a) as well as the transmission factor phase (Fig. 9b) at $\beta_0 = 0$ are in excellent agreement within the investigated range of frequencies. Eq. (24) in combination with the effective surface mass densities of the MAMs based upon the first two symmetric eigenmodes (Eq. (19)) therefore is a suitable method for predicting the normal incidence sound transmission factor of stacked MAMs. In the pressurized cases the same tendencies as in the pressurized single MAM investigations (see Fig. 8) can be observed: With increasing pressure difference β_0 the whole transmission loss spectrum is moved in the direction of higher frequencies.

From Fig. 9c it can be seen that the shifting of the double MAM transmission loss peak follows the same dependence on β_0 as the transmission loss peak of the single MAM given in Fig. 8c, because both stacked MAMs have identical properties. Since the analytical model delivered a slight overprediction of the peak shifting in the single MAM case, the same overprediction can be observed here as well. Still, both numerical and analytical calculations are in very good agreement – even at the highest investigated pressure difference – and it can be concluded that the proposed inflatable double MAM element is suitable for

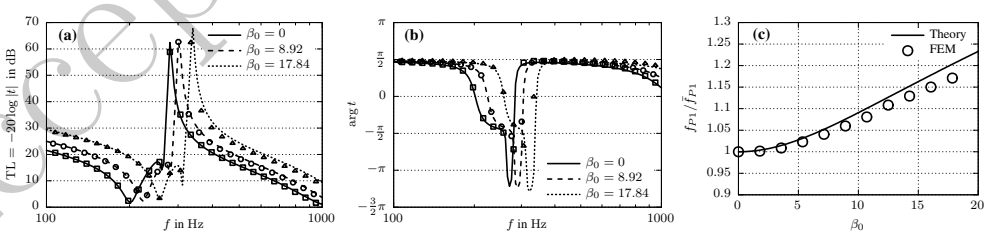

Figure 9: Analytical results (lines) and numerical results (symbols) for the double MAM at different inflation pressure differences β_0. (a) Normal incidence sound transmission loss; (b) Phase of the sound transmission factor t; (c) Shifting of the first transmission loss peak frequency f_{P1}.

adjusting the transmission loss of MAMs during operation.

3. Impedance tube measurements

The present theoretical investigations of the proposed AMAM design are concluded with sound transmission factor measurement results of a test sample obtained inside an impedance tube. The first part of this section gives a brief description of the experimental setup for obtaining the normal incidence sound transmission factor using the 4-microphone technique. Then, a description of the measured test sample and the pressurization method is provided. The third subsection, finally, presents the measurement results at different pressure differences Δp_0 and compares them to the values obtained from the theoretical model that was developed in the previous section.

3.1. Experimental setup

The normal incidence sound transmission factor of the AMAM test sample has been measured inside an impedance tube for different pressurizations Δp_0. The measurement procedure followed the 4-microphone technique based on the transfer matrix method, as described in ASTM E2611-09 [55]. The schematical experimental setup with the impedance tube is shown in Fig. 10. In this setup, a Brüel & Kjær type 4206 impedance tube with a diameter of $D = 100$ mm is used and four $^1/4''$ pressure-field microphones are flush mounted at the tube wall to measure the acoustic pressure inside the tube. The microphone pairs 1 and 2 as well as 3 and 4 are equally spaced with $s = 100$ mm, the spacing between microphones 2 and 3 is given by $l = 350$ mm. This setup allowed a sufficiently accurate measurement of the sound transmission factor in the frequency range from $f = 50$ to 1600 Hz. A loudspeaker driven by a white noise signal generates plane waves that propagate inside the impedance tube. The sample with thickness $H = 15$ mm is mounted inside the tube between the microphones 2 and 3 with the front plane of the sample being positioned at $l_1 = 223$ mm, measured from the location of the second microphone. The microphone signals

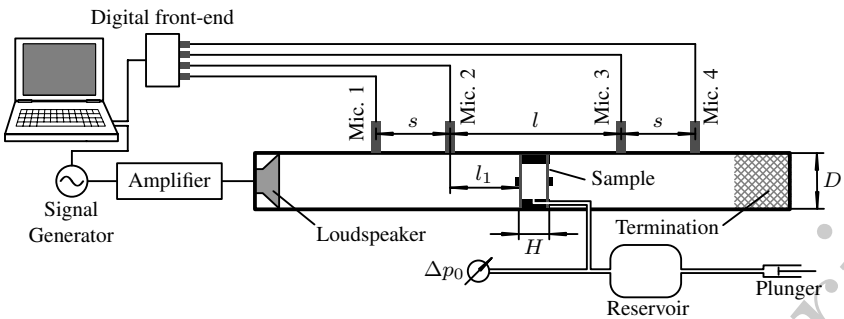

Figure 10: Schematical overview of the experimental setup with the impedance tube and pressurization system.

were collected with a digital data acquisition front-end that was connected to a computer, which calculated the microphone transfer functions H_{11}, H_{21}, H_{31}, and H_{41} by performing a FFT analysis of the acquired microphone time signals. The reference signal for the transfer functions is provided by microphone 1.

According to the two-load method described in ASTM E2611-09 [55], two different termination conditions per sample configuration are required in order to obtain the sample's transmission factor. In the present experiments, the following termination conditions were used: (1) open termination with a 75 mm thick layer of foam at the end of the tube and (2) sound hard. For each termination condition the four microphone transfer functions are measured and the transfer matrix

$$\mathbf{T} = \begin{bmatrix} T_{11} & T_{12} \\ T_{21} & T_{22} \end{bmatrix} \tag{25}$$

is obtained according to ASTM E2611-09 [55] from those measurements. Finally, the sound transmission factor can be obtained from the elements of the transfer matrix using

$$t = \frac{2e^{\mathrm{i}k_0 H}}{T_{11} + \frac{T_{12}}{\rho_0 c_0} + \rho_0 c_0 T_{21} + T_{22}}. \tag{26}$$

3.2. Test sample

A photograph of the measured AMAM sample is shown in Fig. 11a. It consists of a rectangular fibreboard frame with an inner edge length of $L =$

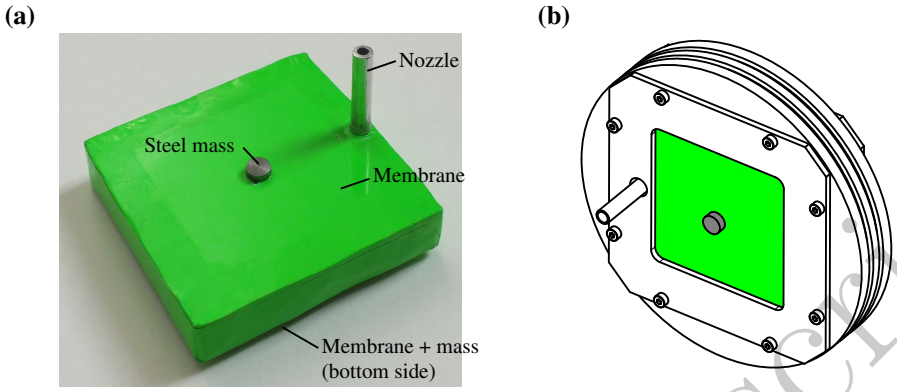

Figure 11: Experimental sample of the proposed AMAM. (a) Photograph of the sample; (b) Drawing of the impedance tube adapter and the AMAM sample positioned inside it.

46 mm and a height of $H = 15$ mm. The membrane material was ironed on onto each side of the frame, thus forming a double membrane unit cell. Then, the membrane material was pre-stressed by using a hot-air blower set at 200 °C. The resulting membrane pre-stress has been determined to be $\bar{T} = 260$ N/m which is slightly higher than the pre-stress in the numerical model, as given in Table 1. However, Eqs. (4), (5), and (18) can still be applied to this sample with the numerically obtained coefficients given in Table 2, because these equations are given in non-dimensional form and the influence of the membrane pre-stress $\bar{T}$ on the eigenfrequency and residual shifting is contained in the non-dimensional static pressure difference β_0, which, in this case, ranges from 0 ($\Delta p_0 = 0$ Pa) to 15.33 ($\Delta p_0 = 1000$ Pa). Finally, identical circular steel masses ($D_M = 6$ mm and $M_1 = M_2 = 0.45$ g) were glued to the center of each membrane, which yielded the proposed double MAM structure shown in Fig. 1. The material properties (except for the pre-stress, which, as explained above, is given by $\bar{T} = 260$ N/m) of both membrane layers and added masses are given in Table 1. Since the impedance tube has a circular cross-section with a diameter of $D = 100$ mm, a test sample adapter made of steel was used to mount the sample inside the impedance tube (see Fig. 11b). The mass of the adapter (0.5 kg) was much larger than the mass of the double MAM element and the edges of the

adapter have been sealed using O-rings and sealing tape to ensure that the sound transmission through the adapter is negligible and acoustic leakage effects are avoided. To account for the smaller size of the sample, the measured transfer matrix elements in Eq. (25) have been corrected with

$$\mathbf{T} = \begin{bmatrix} T_{11} & \sigma T_{12} \\ T_{21}/\sigma & T_{22} \end{bmatrix}, \tag{27}$$

where $\sigma = L^2/(0.25\pi D^2)$ is the ratio of the sample surface area to the cross-sectional area of the tube and zero transmission of sound via the sample adapter is assumed.

The pressurization of the double MAM element is carried out via a tubing that is attached to the sample through a nozzle, which guides the pressurized air via drillings inside the fibreboard frame into the air cavity between the two MAMs. The tubing leaves the impedance tube through a hole in the side wall of the impedance tube and is attached to a T-junction, which connects a pressure sensor for measuring and monitoring the pressure difference Δp_0 and a pressure reservoir to the tubing system (see Fig. 10). The pressurization Δp_0 is kept at a constant value during measurement by manually compensating minor leakages in the setup using a plunger.

3.3. Experimental results

The measured normal incidence sound transmission loss TL and the transmission factor phase of the test sample are shown in Figs. 12a and 12b, respectively, for zero pressurization ($\beta_0 = 0$, solid line) and the highest investigated pressure difference of $\Delta p_0 = 1000$ Pa ($\beta_0 = 15.33$, dotted line). Additionally, theoretical results of the double MAM setup using Eq. (24) with the corresponding expressions for the effective surface mass density as well as the eigenfrequency and residual shifting functions of both MAM layers are given in Fig. 12 (grey curves) to evaluate the capabilities of the analytical model.

At $\beta_0 = 0$ it can be seen that both the measurements as well as the analytical results compare reasonably well. In Fig. 12a, both results exhibit a very sharp

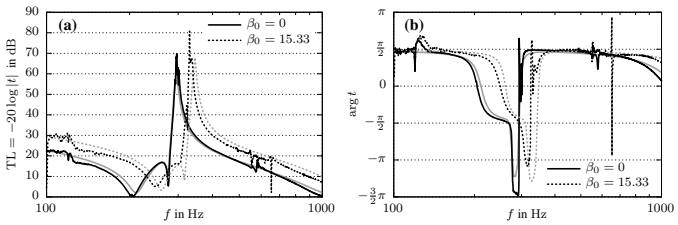

Figure 12: Experimental and theoretical results for the double MAM at two different inflation pressure differences β_0. (a) Normal incidence sound transmission loss; (b) Phase of the sound transmission factor t.

peak with high transmission loss values over 60 dB and then the TL reduces to nearly zero at the second eigenfrequency around 1000 Hz. In case of the results for the transmission factor phase shown in Fig. 12b good agreement between the experimental and analytical results can be observed as well. Around the frequency of the transmission loss peak, where the phase of the transmission factor undergoes a large change, some quantitative differences can be observed which can be attributed to measurement errors due to the high TL values in this frequency band. Nevertheless, the good agreement of these results confirms that the impedance based model in Eq. (24) is suitable for the sound transmission factor calculation of the double MAM arrangement considered here.

In the pressurized case ($\beta_0 = 15.33$) the measured transmission loss shifts to higher frequencies as expected from the theoretical investigations in the previous section. As in the unpressurized case, the qualitative agreement between the measurements and the analytical results is good. The transmission loss peak frequency, however, is slightly overpredicted by the theory. This has already been observed in the comparisons with the FEM simulations and can be linked to the slight inaccuracies of the empirical residual shifting function given in Eq (18). It can be expected that a more thorough theoretical derivation of the shifting functions will further improve the accuracy of the analytical model.

In summary, the experimental results confirm the theoretical results in the previous section. It is possible to adjust the normal incidence sound transmission loss of the AMAM shown in Fig. 1 by applying a suitable pressure difference Δp_0

inside the air cavity between both MAM layers. Given a suitable set of eigenfrequency and residual shifting functions for the first two symmetric eigenmodes of the MAMs, the analytical model is able to provide an accurate prediction of the sound transmission factor of the AMAM for given pressurizations Δp_0.

4. Conclusions

In the present contribution a new design for an adjustable membrane-type acoustic metamaterial was proposed and theoretically, numerically, as well as experimentally investigated. The design consists of two MAM cells separated by an air cavity, which is statically pressurized in order to create large deformations with geometrical stiffening of the MAMs. This effect can be exploited to adjust the eigenmodes and sound transmission loss of the MAMs during operation. The biggest difference of the proposed design compared to other realizations [45, 46] is that no electrical components are necessary near the MAM structures and the adjustment can be controlled centrally using an air pressurization unit (e.g. air conditioning and distribution system). The numerical investigations revealed that two mechanisms are important for the transmission loss adjustment: First, the eigenfrequency shifting, which accounts for the increase of eigenfrequencies due to the geometrical stiffening, and second, the so-called modal residual shifting, which is caused by the change of the mode shapes of the pressurized MAMs. From the simulations it could be concluded that these shiftings are different for each eigenmode and different mass sizes. For analytical normal incidence sound transmission factor calculations using the effective mass density of the MAMs empirical formulas for both shifting mechanisms were derived based upon the numerically obtained data. The analytical models showed a very good agreement with the numerical calculations in both single and double MAM configurations, indicating that the pressurization is a suitable measure for adjusting the sound transmission loss of MAMs. Finally, impedance tube measurements of an inflatable double MAM test sample confirmed the theoretical predictions and the analytical model showed good agreement with the

experimental data.

The analytical models in the present contribution are based upon empirical formula for the eigenfrequency and residual shiftings ϕ_i and χ_i, respectively, which have been fitted to numerical results. Although these equations delivered a very good agreement with the FEM calculations, a more thorough theoretical derivation of these shifting functions based upon an analytical model of the large deflections of pressurized MAMs could deliver additional insights into the influence of several parameters of the MAM on the eigenfrequency and residual shiftings. Also, only the normal incidence sound transmission factor of a single AMAM cell was investigated. In most applications, however, the incident sound fields are diffuse and large surfaces need to be covered with multiple parallel AMAM cells. Therefore, subsequent investigations of the proposed AMAMs should consider the diffuse field sound transmission loss of large-scale structures. Some recent investigations [27, 36, 37] suggest that the normal incidence properties of a single AMAM cell can be transferred to more realistic conditions.

In addition, the transmission loss adjustment of the AMAM cell could be further improved by allowing the pressure inside the air cavity to be adjusted dynamically. With a microphone positioned on the transmission side of the AMAM measuring the transmitted sound pressure level and a suitable controller that dynamically actuates the pressure inside the AMAM air cavity to generate sound waves cancelling out the transmitted sound wave, the sound transmission factor of the AMAM could be – in theory – modified nearly arbitrarily.

Acknowledgements

This work has been performed under the framework of the LuFo IV-4 project Comfortable Cabin for Low-Emission Aircraft (COCLEA), funded by the Federal Ministry for Economic Affairs and Energy (grant number: 20K1102D). The financial support is gratefully acknowledged by the authors.

Appendix A. Impedance based calculation of the double MAM sound transmission factor

This section provides a theoretical background for the derivation of Eq. (23), where the normal incidence sound transmission factor t of a double MAM element is obtained using the effective surface mass densities $\widetilde{m}_1''$ and $\widetilde{m}_2''$ of both MAM layers coupled by the sealed air cavity with height H between the MAMs.

In the basic setup of the fully coupled vibro-acoustic problem, as shown in Fig. A.13, the double MAM element is positioned inside a rectangular acoustic waveguide with edge length L and sound-hard side walls. Both ends of the waveguide are presumed to be non-reflecting so that the acoustic pressure amplitude field inside the incident side fluid cavity $\hat{p}_1(x,y,z)$ is given by [56]

$$\hat{p}_1(x,y,z) = \hat{p}_i e^{-\mathrm{i}k_0 z} + \sum_{p=0}^{\infty}\sum_{q=0}^{\infty} \hat{p}_{r,pq} \cos(k_p x)\cos(k_q y)\, e^{\mathrm{i}k_{pq} z}, \tag{A.1}$$

where $\hat{p}_i$ is the amplitude of the incident plane acoustic wave, $\hat{p}_{r,pq}$ are the amplitudes of the reflected waveguide modes, given by the indices p and q as well as the lateral wavenumbers $k_p = \pi p/L$ and $k_q = \pi q/L$, and $k_{pq} = \sqrt{k_0^2 - k_p^2 - k_q^2}$ is the modal wavenumber component in z-direction. By splitting up the double infinite sum into a zero order part, i.e. the reflected plane wave with amplitude $\hat{p}_r$, and a higher order part, Eq. (A.1) can be written as

$$\hat{p}_1(x,y,z) = \hat{p}_i e^{-\mathrm{i}k_0 z} + \hat{p}_r e^{\mathrm{i}k_0 z} + \delta\hat{p}_r, \tag{A.2}$$

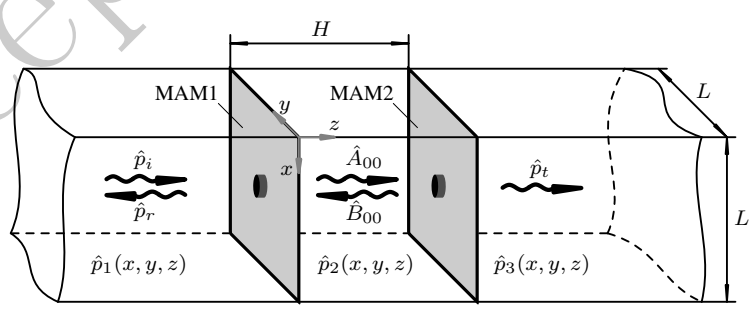

Figure A.13: Geometrical setup and definitions for the theoretical derivation of the impedance based double MAM element model.

where $\delta\hat{p}_r$ is the higher order reflected pressure field given by

$$\delta\hat{p}_r = \hat{p}_{r,10}\cos(k_1 x)\, e^{\mathrm{i}k_{10}z} + \hat{p}_{r,01}\cos(k_1 y)\, e^{\mathrm{i}k_{01}z} + \sum_{p=1}^{\infty}\sum_{q=1}^{\infty}\hat{p}_{r,pq}\cos(k_p x)\cos(k_q y)\, e^{\mathrm{i}k_{pq}z}. \tag{A.3}$$

Similarly, the pressure field transmitted through the double MAM $\hat{p}_3(x,y,z)$ is given by

$$\hat{p}_3(x,y,z) = \hat{p}_t e^{-\mathrm{i}k_0 z} + \delta\hat{p}_t, \tag{A.4}$$

where $\hat{p}_t$ is the transmitted plane acoustic wave amplitude and the higher order transmitted pressure field $\delta\hat{p}_t$ is

$$\delta\hat{p}_t = \hat{p}_{t,10}\cos(k_1 x)\, e^{-\mathrm{i}k_{10}z} + \hat{p}_{t,01}\cos(k_1 y)\, e^{-\mathrm{i}k_{01}z} + \sum_{p=1}^{\infty}\sum_{q=1}^{\infty}\hat{p}_{t,pq}\cos(k_p x)\cos(k_q y)\, e^{-\mathrm{i}k_{pq}z}, \tag{A.5}$$

with the amplitudes $\hat{p}_{t,pq}$ of the higher order transmitted waves. Because the edge length L of the MAMs considered here is much smaller than the smallest wavelength inside the frequency range of interest, the higher order normal wavenumbers k_{pq} are imaginary in this frequency range and therefore the higher order reflected and transmitted pressure fields consist only of evanescent waves which do not transport acoustic energy into the far-field [12]. Thus, the normal incidence sound transmission factor $t = \hat{p}_t/\hat{p}_i$ can be used to characterize the sound power transmitted through the double MAM element.

The pressure field $\hat{p}_2(x,y,z)$ inside the sealed cavity between the two MAM layers can be written as

$$\hat{p}_2(x,y,z) = \sum_{p=0}^{\infty}\sum_{q=0}^{\infty}\cos(k_p x)\cos(k_q y)\left(\hat{A}_{pq}e^{-\mathrm{i}k_{pq}z} + \hat{B}_{pq}e^{\mathrm{i}k_{pq}z}\right) = \hat{A}_{00}e^{-\mathrm{i}k_0 z} + \hat{B}_{00}e^{\mathrm{i}k_0 z} + \delta\hat{p}_2, \tag{A.6}$$

where the field has been split into a part with plane waves propagating in positive and negative z-direction with amplitudes $\hat{A}_{00}$ and $\hat{B}_{00}$, respectively, (see Fig. A.13) as well as an evanescent wave field $\delta\hat{p}_2$.

The z-components of the particle velocity inside those three fluid regions are

given by

$$\hat{v}_{z1}(x,y,z) = -\frac{1}{\mathrm{i}\omega\rho_0}\frac{\partial p_1}{\partial z} = \frac{\hat{p}_i}{\rho_0 c_0}e^{-\mathrm{i}k_0 z} - \frac{\hat{p}_r}{\rho_0 c_0}e^{\mathrm{i}k_0 z} + \delta\hat{v}_{z,r}, \tag{A.7}$$

$$\hat{v}_{z2}(x,y,z) = -\frac{1}{\mathrm{i}\omega\rho_0}\frac{\partial p_2}{\partial z} = \frac{\hat{A}_{00}}{\rho_0 c_0}e^{-\mathrm{i}k_0 z} - \frac{\hat{B}_{00}}{\rho_0 c_0}e^{\mathrm{i}k_0 z} + \delta\hat{v}_{z2}, \quad \text{and} \tag{A.8}$$

$$\hat{v}_{z3}(x,y,z) = -\frac{1}{\mathrm{i}\omega\rho_0}\frac{\partial p_3}{\partial z} = \frac{\hat{p}_t}{\rho_0 c_0}e^{-\mathrm{i}k_0 z} + \delta\hat{v}_{z,t}, \tag{A.9}$$

where $\delta\hat{v}_{z,r}$, $\delta\hat{v}_{z2}$, and $\delta\hat{v}_{z,t}$ correspond to the particle velocities of the evanescent fields within each cavity, respectively. The velocity amplitudes of the MAMs, on the other hand, can be expressed as

$$\hat{v}_{z,\mathrm{MAM1}}(x,y) = \langle\hat{v}_{z,\mathrm{MAM1}}\rangle + \delta\hat{v}_{z,\mathrm{MAM1}} \quad \text{and} \tag{A.10}$$

$$\hat{v}_{z,\mathrm{MAM2}}(x,y) = \langle\hat{v}_{z,\mathrm{MAM2}}\rangle + \delta\hat{v}_{z,\mathrm{MAM2}}, \tag{A.11}$$

with $\langle\hat{v}\rangle$ representing the surface averaged part of the velocity amplitude and $\delta\hat{v}$ denoting the spatially varying deviation from the surface average. Using the definition of the effective surface mass density in Eq. (7), these expressions can be rewritten as

$$\hat{v}_{z,\mathrm{MAM1}}(x,y) = \frac{\langle\Delta\hat{p}_{\mathrm{MAM1}}\rangle}{\mathrm{i}\omega\widetilde{m}_1''} + \delta\hat{v}_{z,\mathrm{MAM1}} \quad \text{and} \tag{A.12}$$

$$\hat{v}_{z,\mathrm{MAM2}}(x,y) = \frac{\langle\Delta\hat{p}_{\mathrm{MAM2}}\rangle}{\mathrm{i}\omega\widetilde{m}_2''} + \delta\hat{v}_{z,\mathrm{MAM2}}. \tag{A.13}$$

The surface averaged pressure differences along the MAMs are given by

$$\langle\Delta\hat{p}_{\mathrm{MAM1}}\rangle = \langle\hat{p}_1 - \hat{p}_2\rangle|_{z=0} = \hat{p}_i + \hat{p}_r - \hat{A}_{00} - \hat{B}_{00} \quad \text{and} \tag{A.14}$$

$$\langle\Delta\hat{p}_{\mathrm{MAM2}}\rangle = \langle\hat{p}_2 - \hat{p}_3\rangle|_{z=H} = e^{-\mathrm{i}k_0 H}\hat{A}_{00} + e^{\mathrm{i}k_0 H}\hat{B}_{00} - e^{-\mathrm{i}k_0 H}\hat{p}_t, \tag{A.15}$$

respectively, because the surface average of the higher order pressure fields $\delta\hat{p}_r$, $\delta\hat{p}_2$, and $\delta\hat{p}_t$ is zero.

For the coupling between the two MAM layers and the fluid domains, the

continuity of the velocity amplitudes at the MAM layer surfaces is required with

$$\frac{\langle \Delta\hat{p}_{\mathrm{MAM1}}\rangle}{\mathrm{i}\omega\widetilde{m}_1''} + \delta\hat{v}_{z,\mathrm{MAM1}} = \frac{\hat{p}_i}{\rho_0 c_0} - \frac{\hat{p}_r}{\rho_0 c_0} + \delta\hat{v}_{z,r}|_{z=0}, \tag{A.16}$$

$$\frac{\langle \Delta\hat{p}_{\mathrm{MAM1}}\rangle}{\mathrm{i}\omega\widetilde{m}_1''} + \delta\hat{v}_{z,\mathrm{MAM1}} = \frac{\hat{A}_{00}}{\rho_0 c_0} - \frac{\hat{B}_{00}}{\rho_0 c_0} + \delta\hat{v}_{z2}|_{z=0}, \tag{A.17}$$

$$\frac{\langle \Delta\hat{p}_{\mathrm{MAM2}}\rangle}{\mathrm{i}\omega\widetilde{m}_2''} + \delta\hat{v}_{z,\mathrm{MAM2}} = \frac{\hat{A}_{00}}{\rho_0 c_0} e^{-\mathrm{i}k_0 H} - \frac{\hat{B}_{00}}{\rho_0 c_0} e^{\mathrm{i}k_0 H} + \delta\hat{v}_{z2}|_{z=H}, \quad \text{and} \tag{A.18}$$

$$\frac{\langle \Delta\hat{p}_{\mathrm{MAM2}}\rangle}{\mathrm{i}\omega\widetilde{m}_2''} + \delta\hat{v}_{z,\mathrm{MAM2}} = \frac{\hat{p}_t}{\rho_0 c_0} e^{-\mathrm{i}k_0 H} + \delta\hat{v}_{z,t}|_{z=H}. \tag{A.19}$$

Since the surface average of the higher order parts is, by definition, zero, the plane wave and higher order wave parts in the continuity conditions (A.16) to (A.19) can be considered separately [32]. Therefore, using Eqs. (A.14) and (A.15) as well as the definition for the non-dimensional wall impedance in Eq. (22) the velocity amplitude continuity conditions are rewritten as

$$\frac{\hat{p}_i + \hat{p}_r - \hat{A}_{00} - \hat{B}_{00}}{2X_1} = \hat{p}_i - \hat{p}_r, \tag{A.20}$$

$$\frac{\hat{p}_i + \hat{p}_r - \hat{A}_{00} - \hat{B}_{00}}{2X_1} = \hat{A}_{00} - \hat{B}_{00}, \tag{A.21}$$

$$\frac{e^{-\mathrm{i}k_0 H}\hat{A}_{00} + e^{\mathrm{i}k_0 H}\hat{B}_{00} - e^{-\mathrm{i}k_0 H}\hat{p}_t}{2X_2} = e^{-\mathrm{i}k_0 H}\hat{A}_{00} - e^{\mathrm{i}k_0 H}\hat{B}_{00}, \quad \text{and} \tag{A.22}$$

$$\frac{e^{-\mathrm{i}k_0 H}\hat{A}_{00} + e^{\mathrm{i}k_0 H}\hat{B}_{00} - e^{-\mathrm{i}k_0 H}\hat{p}_t}{2X_2} = e^{-\mathrm{i}k_0 H}\hat{p}_t, \tag{A.23}$$

for the plane wave parts of the acoustic pressure fields, and

$$\delta\hat{v}_{z,\mathrm{MAM1}} = \delta\hat{v}_{z,r}|_{z=0} = \delta\hat{v}_{z2}|_{z=0} \quad \text{and} \tag{A.24}$$

$$\delta\hat{v}_{z,\mathrm{MAM2}} = \delta\hat{v}_{z2}|_{z=H} = \delta\hat{v}_{z,t}|_{z=H}, \tag{A.25}$$

for the higher order acoustic pressure fields. Eqs. (A.20) to (A.23) form a linear system of equations for the four unknown pressure amplitudes $\hat{p}_r$, $\hat{p}_t$, $\hat{A}_{00}$, and $\hat{B}_{00}$, which can be solved for the transmitted pressure amplitude $\hat{p}_t$ to yield the following expression for the sound transmission factor

$$t = \frac{\hat{p}_t}{\hat{p}_i} = \frac{1}{1 + X_1 + X_2 + X_1 X_2 \left(1 - e^{-2\mathrm{i}k_0 H}\right)}, \tag{A.26}$$

which is equivalent to the expression given in Eq. (23).

[1] B. Banerjee, An Introduction to Metamaterials and Waves in Composites, Taylor & Francis, 2011.

[2] J. B. Pendry, A. J. Holden, W. J. Stewart, I. Youngs, Extremely low frequency plasmons in metallic mesostructures, Physical Review Letters 76 (1996) 4773–4776.

[3] J. B. Pendry, A. J. Holden, D. J. Robbins, W. J. Stewart, Magnetism from conductors and enhanced nonlinear phenomena, IEEE Transactions on Microwave Theory and Techniques 47 (1999) 2075–2084.

[4] D. R. Smith, W. J. Padilla, D. C. Vier, S. C. Nemat-Nasser, S. Schultz, Composite medium with simultaneously negative permeability and permittivity, Physical Review Letters 84 (2000) 4184–4187.

[5] R. A. Shelby, D. R. Smith, S. Schultz, Experimental verification of a negative index of refraction, Science 292 (2001) 77–79.

[6] V. G. Veselago, The electrodynamics of substances with simultaneously negative values of ϵ and μ, Soviet Physics Uspekhi 10 (1968) 509–514.

[7] J. B. Pendry, Negative refraction makes a perfect lens, Physical Review Letters 85 (2000) 3966–3969.

[8] D. Schurig, J. J. Mock, B. J. Justice, S. A. Cummer, J. B. Pendry, A. F. Starr, D. R. Smith, Metamaterial electromagnetic cloak at microwave frequencies, Science 314 (2006) 977–980.

[9] Z. Liu, X. Zhang, Y. Mao, Y. Y. Zhu, Z. Yang, C. T. Chan, P. Sheng, Locally resonant sonic materials, Science 289 (2000) 1734–1736.

[10] Z. Liu, C. T. Chan, P. Sheng, Analytic model of phononic crystals with local resonances, Physical Review B 71 (2005) 014103.

[11] K. M. Ho, C. K. Cheng, Z. Yang, X. X. Zhang, P. Sheng, Broadband locally resonant sonic shields, Applied Physics Letters 83 (2003) 5566–5568.

[12] Z. Yang, J. Mei, M. Yang, N. H. Chan, P. Sheng, Membrane-type acoustic metamaterial with negative dynamic mass, Physical Review Letters 101 (2008) 204301.

[13] S. H. Lee, C. M. Park, Y. M. Seo, Z. G. Wang, C. K. Kim, Acoustic metamaterial with negative density, Physics Letters A 373 (2009) 4464–4469.

[14] S. Yao, X. Zhou, G. Hu, Investigation of the negative-mass behaviors occurring below a cut-off frequency, New Journal of Physics 12 (2010) 103025.

[15] Y. Xiao, J. Wen, X. Wen, Sound transmission loss of metamaterial-based thin plates with multiple subwavelength arrays of attached resonators, Journal of Sound and Vibration 331 (2012) 5408–5423.

[16] N. Sui, X. Yan, T.-Y. Huang, J. Xu, F.-G. Yuan, Y. Jing, A lightweight yet sound-proof honeycomb acoustic metamaterial, Applied Physics Letters 106 (2015) 171905.

[17] N. Fang, D. Xi, J. Xu, M. Ambati, W. Srituravanich, C. Sun, X. Zhang, Ultrasonic metamaterials with negative modulus, Nature Materials 5 (2006) 452–456.

[18] S. H. Lee, C. M. Park, Y. M. Seo, Z. G. Wang, C. K. Kim, Acoustic metamaterial with negative modulus., Journal of Physics: Condensed Matter 21 (2009) 175704.

[19] C. Ding, L. Hao, X. Zhao, Two-dimensional acoustic metamaterial with negative modulus, Journal of Applied Physics 108 (2010) 074911.

[20] J. Fey, W. M. Robertson, Compact acoustic bandgap material based on a subwavelength collection of detuned helmholtz resonators, Journal of Applied Physics 109 (2011) 114903.

[21] J. Li, C. T. Chan, Double-negative acoustic metamaterial, Physical Review E 70 (2004) 055602.

[22] S. Guenneau, A. Movchan, G. Pétursson, S. A. Ramakrishna, Acoustic metamaterials for sound focusing and confinement, New Journal of Physics 9 (2007) 399.

[23] S. H. Lee, C. M. Park, Y. M. Seo, Z. G. Wang, C. K. Kim, Composite acoustic medium with simultaneously negative density and modulus, Physical Review Letters 104 (2010) 054301.

[24] M. Yang, G. Ma, Z. Yang, P. Sheng, Coupled membranes with doubly negative mass density and bulk modulus, Physical Review Letters 110 (2013) 134301.

[25] B. Liang, B. Yuan, J.-C. Cheng, Acoustic diode: Rectification of acoustic energy flux in one-dimensional systems, Physical Review Letters 103 (2009) 104301.

[26] S. Zhang, C. Xia, N. Fang, Broadband acoustic cloak for ultrasound waves, Physical Review Letters 106 (2011) 024301.

[27] J. Mei, G. Ma, M. Yang, Z. Yang, W. Wen, P. Sheng, Dark acoustic metamaterials as super absorbers for low-frequency sound, Nature Communications 3 (2012) 756.

[28] J. J. Park, C. M. Park, K. J. B. Lee, S. H. Lee, Acoustic superlens using membrane-based metamaterials, Applied Physics Letters 106 (2015) 051901.

[29] Z. Yang, H. M. Dai, N. H. Chan, G. C. Ma, P. Sheng, Acoustic metamaterial panels for sound attenuation in the 50–1000 Hz regime, Applied Physics Letters 96 (2010) 041906.

[30] C. J. Naify, C.-M. Chang, G. McKnight, S. Nutt, Transmission loss and dynamic response of membrane-type locally resonant acoustic metamaterials, Journal of Applied Physics 108 (2010) 114905.

[31] Y. Zhang, J. Wen, Y. Xiao, X. Wen, J. Wang, Theoretical investigation of the sound attenuation of membrane-type acoustic metamaterials, Physics Letters A 376 (2012) 1489–1494.

[32] Y. Chen, G. Huang, X. Zhou, G. Hu, C.-T. Sun, Analytical coupled vibroacoustic modeling of membrane-type acoustic metamaterials: Membrane model, The Journal of the Acoustical Society of America 136 (2014) 969–979.

[33] F. Langfeldt, W. Gleine, O. von Estorff, Analytical model for low-frequency transmission loss calculation of membranes loaded with arbitrarily shaped masses, Journal of Sound and Vibration 349 (2015) 315–329.

[34] C. J. Naify, C.-M. Chang, G. McKnight, S. Nutt, Transmission loss of membrane-type acoustic metamaterials with coaxial ring masses, Journal of Applied Physics 110 (2011) 124903.

[35] H. Tian, X. Wang, Y.-H. Zhou, Theoretical model and analytical approach for a circular membrane-ring structure of locally resonant acoustic metamaterial, Applied Physics A 114 (2013) 985–990.

[36] C. J. Naify, C.-M. Chang, G. McKnight, S. R. Nutt, Scaling of membrane-type locally resonant acoustic metamaterial arrays, The Journal of the Acoustical Society of America 132 (2012) 2784–92.

[37] C. J. Naify, C.-M. Chang, G. McKnight, F. Scheulen, S. Nutt, Membrane-type metamaterials: Transmission loss of multi-celled arrays, Journal of Applied Physics 109 (2011) 104902.

[38] Y. Zhang, J. Wen, H. Zhao, D. Yu, L. Cai, X. Wen, Sound insulation property of membrane-type acoustic metamaterials carrying different masses at adjacent cells, Journal of Applied Physics 114 (2013) 063515.

[39] A. Baz, The structure of an active acoustic metamaterial with tunable effective density, New Journal of Physics 11 (2009) 123010.

[40] A. Baz, An active acoustic metamaterial with tunable effective density, Journal of Vibration and Acoustics 132 (2010) 041011.

[41] W. Akl, A. Baz, Multi-cell active acoustic metamaterial with programmable bulk modulus, Journal of Intelligent Material Systems and Structures 21 (2010) 541–556.

[42] W. Akl, A. Baz, Analysis and experimental demonstration of an active acoustic metamaterial cell, Journal of Applied Physics 111 (2012) 044505.

[43] B.-I. Popa, L. Zigoneanu, S. A. Cummer, Tunable active acoustic metamaterials, Physical Review B 88 (2013) 024303.

[44] B.-I. Popa, S. A. Cummer, Non-reciprocal and highly nonlinear active acoustic metamaterials, Nature Communications 5 (2014) 3398.

[45] X. Chen, X. Xu, S. Ai, H. Chen, Y. Pei, X. Zhou, Active acoustic metamaterials with tunable effective mass density by gradient magnetic fields, Applied Physics Letters 105 (2014) 071913.

[46] S. Xiao, G. Ma, Y. Li, Z. Yang, P. Sheng, Active control of membrane-type acoustic metamaterial by electric field, Applied Physics Letters 106 (2015) 091904.

[47] R. H. Plaut, Linearly elastic annular and circular membranes under radial, transverse, and torsional loading. part II: Vibrations about deformed equilibria, Acta Mechanica 202 (2009) 101–110.

[48] A. M. Eriksson, D. Midtvedt, A. Croy, A. Isacsson, Frequency tuning, nonlinearities and mode coupling in circular mechanical graphene resonators, Nanotechnology 24 (2013) 395702.

[49] C. H. Jenkins, Nonlinear dynamic response of membranes: state of the art-update, Applied Mechanics Reviews 49 (1996) S41–S48.

[50] M. Yang, G. Ma, Y. Wu, Z. Yang, P. Sheng, Homogenization scheme for acoustic metamaterials, Physical Review. B 89 (2014) 064309.

[51] W. Soedel, Vibrations of shells and plates, 3rd ed., Marcel Dekker, Inc., New York, 2004.

[52] R. H. Plaut, Linearly elastic annular and circular membranes under radial, transverse, and torsional loading. part I: large unwrinkled axisymmetric deformations, Acta Mechanica 202 (2009) 79–99.

[53] M. Long, Architectural Acoustics, Elsevier, Burlington, 2005.

[54] M. Yang, C. Meng, C. Fu, Y. Li, Z. Yang, P. Sheng, Subwavelength total acoustic absorption with degenerate resonators, Applied Physics Letters 107 (2015) 104104.

[55] American Society for Testing and Materials ASTM E2611-09, Standard test method for measurement of normal incidence sound transmission of acoustical materials based on the transfer matrix method, 2009.

[56] M. Möser, Technische Akustik, volume 8, Springer, 2009.